Results

Single molecular imaging of breast cancer by semiconductor quantum dots conjugated with anti-HER2 antibody

The molar ratio of trastuzumab to the Qdots of the QT complexes was approximately 3:1. KPL-4 cell membrane and QT complexes strongly bound 5 min after mixture of KPL-4 and 10-nM QT complexes. Six hours after the mixing, the signals from the QT complexes were found mainly in the cytosol neighboring the nucleus, suggesting that the QT complexes were endocytosed. Qdots without trastuzumab did not bind or accumulate in the KPL-4 cells. A control study using AH109A cells, a HER2 negative cell line, also showed no binding of the QT complexes, indicating that QT complexes selectively bind to the HER2 protein.

A tumor-bearing mice model was prepared with subcutaneous implantation of KPL-4. A single Qdot in the tumor-bearing mice was observed using a high-resolution intravital imaging system through the DSFC. This system captures images of single Qdots at a video rate of 33 ms per frame. The DSFC was firmly mounted on the microscope stage to minimize the distorting influence of the heartbeat and breathing. 3D confocal intravital images of single QT complexes were taken by moving an objective lens. 3D images of the tumor were taken by reconstructing 10–20 confocal images from the surface of the mice to a depth of 150 mm inside the tumor through the DSFC. Fluorescence micro-angiography was performed after injection of the QT complexes into the tail vein. The membranes of the KPL-4 tumor cells were clearly stained with QT complexes at 6 h after the injection. Up to 24 h after the injection, the QT complexes had been internalized into and increased in the tumor cells.

After in vivo tumor imaging of the mice, histological examination of the chemically fixed tumors was performed to confirm that QT complexes in the living mice exhibit activity on the KPL-4 cells. QT complexes observed under the 3D microscope were located at the cell membrane and near the nuclear membrane. The position of the objective was fixed and 300–3,000 sequential confocal 2D images (total 10–100 s) were taken at this fixed position. Within 30 s after the injection, the current of the QT complex in a vessel was observed. When we could observe a vessel and cells clearly, the single QT complex in the current of the tumor vessel was then analyzed. The fluorescence image of the circulating QT complexes was not a circle but an ellipse and sometimes a line at the video rate because QT complexes at times moved >1 mm in a single frame. The speed of the movement of the single particles was calculated from the positional changes of the centroid of the QT complex images. The average speed of each complex ranged from 100 to 600 μm/s, in agreement with a previous report by another method [14]. Each particle exhibited slow and fast movement in the bloodstream. Such fast and slow movement characteristics could be induced by the pulse and nonuniform current within a vessel such as the Hagen–Poiseuille current. The slow speed of the complexes inside a tumor vessel would be important to locate pores between the vessel cells and then moved out through these pores.

Focusing on the vessel walls, a movement was observed of the QT complex extravasated from the intravascular space. The edge of the vascular inner surface was not clear on a single-frame image. Therefore, all the images obtained were averaged to precisely determine the position of the edge. The complexes were positioned first on the vascular surface and then extravasated. This is the first example of video rate observation of extravasation of nanoparticles, such as Qdots, in a mouse model.

Two hours after the injection, many complexes had migrated into the tumor interstitial area close to the tumor vessels. Most of the movement of the complexes was random in both orientation and speed, indicating that complexes diffuse by the Brownian motion exerted by thermal energy. The average diffusion coefficient of the complexes was 0.0014 mm^2/s, much smaller than that at free diffusion in solution (~ 10 mm^2/s). Many complexes also moved randomly within a restricted small area of ~ 1 mm in diameter and then hopped by ~ 1 mm. The movement was restricted by a cage formed by the extracellular matrix.

Six hours after the injection, QT complexes had bound to the KPL-4 cell membrane on which the HER2 protein is located. We successfully captured specific images of the QT complexes bound to the cell membrane. Movements of a single QT complex are identified in single frames. To identify the positions of the tumor vessels and cells in living mice without further fluorescence staining, images were averaged. Many QT complexes bound to the cell membrane exhibited Brownian motion within a restricted region of ~ 500 nm in diameter. This region is significantly larger than the area of ~ 30 nm, which was drawn by position noise of the complexes fixed on a coverslip, indicating the movement is due to the anchor of the HER2 to a flexible component of the cytoskeleton such as an actin filament [15]. The QT complexes restricted to the small area initiated linear movement in one direction along the cell membrane with speed of 400–600 nm/s and traveled for several micrometers.

We also observed in pursuing the transport of QT complexes from the peripheral region of the cell to the perinuclear region. The QT complex in a given cell moved almost straight towards the cell membrane with a velocity of 100–300 nm/s, changed direction to parallel to

the cell membrane, and moved toward the cell nucleus at a velocity of ~600 nm/s. Finally, the directional movement of the QT complex ceased and Brownian motion commenced within a small area, ~1 μm in a diameter, near the nucleus. The first two movements, straight towards and along the cell membrane, would most likely be produced by the transport of an acto-myosin system binding to vesicle containing QT complexes [16], because the actin filaments in cultured cells are highly concentrated in the peripheral region of cells. Movement towards the nucleus would most likely be on a microtubule transported by dynein [17] since there are almost no actin filaments near the nucleus, but rather, a high concentration of microtubules.

Sentinel node navigation by nanosized fluorescent beads

We performed the experiment on four types of beads with diameters of 20, 40, 100, and 200 nm. In the experiment using 20-nm beads, 22 ft from 13 rats were tested. SNs were detected in 10 ft of 22 (45%) by fluorescence contrast as shown in Fig. 3. The time of detection from injection was 0–6 min. The average time for detection was 2.5 min and the median time was 2 min. With the 40-nm beads, SNs were detected in 50 of 72 ft (69%). The time of detection from injection was 0 to 28 min. SNs in 42 ft were detected within 5 min. They were the most representative cases (84%). The average time was 4.6 min and the median time was 3 min. With 100-nm beads, SNs were detected in two of 10 ft (20%). The average and median times were both 56 min. With the 200-nm beads, SNs were detected in seven of 18 ft (39%). The average time was 127 min. The median time was 135 min. In the 40- and 20-nm experiments, there was a significant difference in both the positive rate and average time. In the same way, we compared 40 with 100- or 200-nm beads.

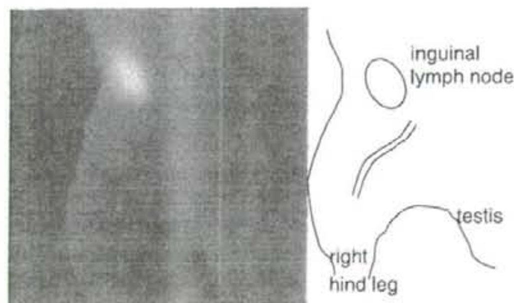

Fig. 3 Fluorescence image of right inguinal node and its illustration for sentinel node imaging using nanosized fluorescent particle in rat

We investigated three excitation and emission wavelengths with the 40-nm beads, yellow–green (YG), dark red (DR) and infrared (IR). Beads of 40 nm in diameter were found to be the most suitable size in the previous experiment. In the experiment using YG, 10 ft from five rats were tested. SNs in three of 10 ft (30%) were observed by fluorescence measurement. With DR, SNs in 24 of 31 ft (77%) were observed and with IR, SNs in 23 of 31 ft (74%) were observed. DR and IR have advantage of positive rate of fluorescence detection as compared with YG.

In these experiments, four different fluorescent wavelengths 515, 680, 720, and 755 nm were studied. DR and IR were more sensitive than YG in the detection rate experiments with 40 nm. There was no significant difference in detection rate, but in average time between DR and IR. However, spectral analysis of DR and IR showed that IR has a higher signal-to-noise ratio compared to DR.

Discussion

In the study for single molecular imaging of cancer, we captured the specific delivery of single QT complexes in tumor vessels to the perinuclear region of tumor cells in live mice after QT complexes had been injected into the tail vein of mice. Six stages were detected (Fig. 4), (1) vessel circulation, (2) extravasation, (3) movement into the extracellular region, (4) binding to HER2 on the cell membrane, (5) movement from the cell membrane to the perinuclear region after endocytosis and (6) in the perinuclear region. The transport speed of QT complexes in each process was highly variable, even in the vessel circulation. The movement of the complexes in each process was also found to be "stop-and-go", i.e., the complex remaining within a highly restricted area and then moving suddenly. This indicates that the movement was promoted by a motive power and constrained by both the 3D structure and protein-protein interactions. The motive power of the movements was produced by blood circulation (essential in processes 1 and 2), diffusion force driven by thermal energy (2, 3 and 4) and active transport by motor proteins (5). The cessation of movement is most likely induced by a structural barricade such as a matrix cage (2, 3, and 4) and/or specific interaction between proteins, e.g., an antibody and HER2 (4), motor proteins, and rail filaments such as actin filaments and microtubules (5).

The molecular mechanism underlying the movement and its cessation during delivery of nanoparticles in animal models is the fundamental basis of drug delivery. There have been many different approaches to tumor-targeting "nanocarriers" including anti-cancer drugs, for passive targeting such as Myocet [18], Doxil [19] and for active targeting such as MCC-465 [20], anti-HER2

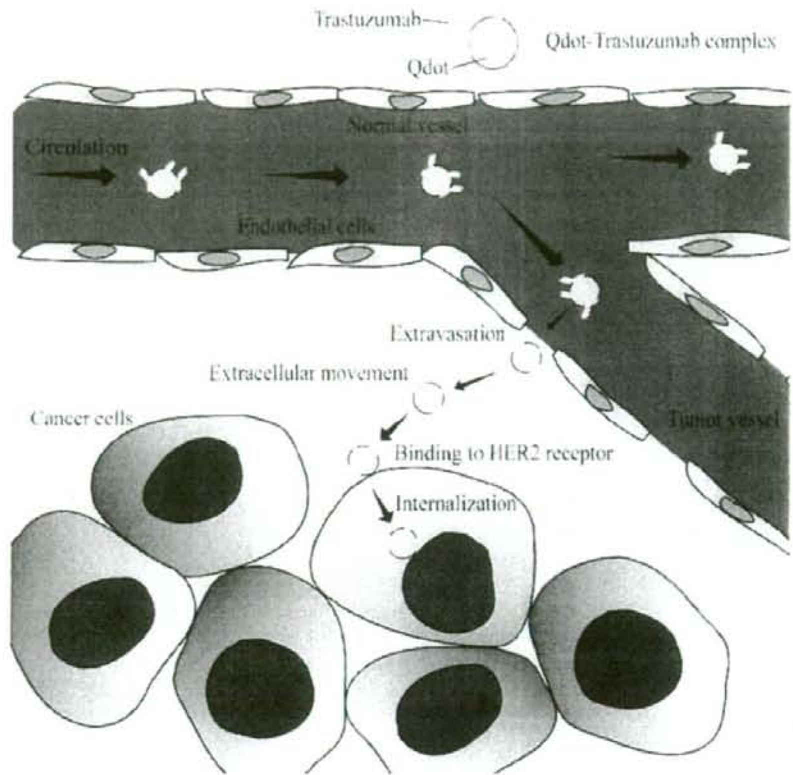

Fig. 4 Delivery of the quantum dots labeled monoclonal antibody. The QT complex in the circulation moved vessel to the interstitial space then bound to the tumor cells. The QT complex finally reached at the nuclear region through intracellular rail protein

immunoliposome [21]. There is still very little understanding of the biological behavior of nanocarriers, including such crucial features as their transport in the blood circulation, cellular recognition, translocation into the cytoplasm, and final fate in the target cell. These results suggest that the transport of nanocarriers would be quantitatively analyzable in the tumors of living animals by the present method. This approach thus should afford great potential new insight into particle behavior in complex biological environments. Such new insight in turn will allow rational improvements in particle design to increase the therapeutic index of the tumor targeting nanocarriers.

Nanocrystal semiconductor quantum dots conjugated with antibody may serve fundamentally as new controllable materials for medical purposes including cancer molecular imaging.

Homogeneous nanosized beads have shown an advantage for efficient SN detection compared to existing colloids agents of heterogeneous size in the fluorescent nanoparticle study for sentinel navigation surgery. Although the appropriate size for SN detection for human beings is predicted to be 500 nm, and the optimum size may be different between animal species, the appropriate size should be determined for humans with accurately measured nanosized beads of strictly same dimensions. There are two forms of transportation mechanism regarding a particle material to lymphatic system that is injected into tissue space. One is physical and active extracellular transportation; a particle passes through lymph capillaries. The other one is intracellular transportation of a particle. Foreign materials shift to the lymph capillaries after phagocytosis of particle. An investigation of in vivo dynamics of tracers is important in SN biopsy. It is reported that lymph node was detected by protected graft copolymer combined with Cy5.5, or methoxypolyethyleneglycol-poly-L-lysine combined with Cy5.5 as a tracer. The nanoparticle may distribute to reticuloendothelial system as described in previous reports [22, 23], or may be excreted from kidney for their hydrophilia. We histologically observed liver and kidney 2 weeks after subcutaneous injection of fluorescent beads. Consequently, we did not find beads trapped in liver or kidney by fluorescent microscopic observation, suggesting that the safety of these beads would be ensured when they are given in vivo.

The fluorescent beads that we used are mainly consisted of polystyrene. As polystyrene is the material often used for surgical strings in operation, it would be safe to gave fluorescent beads to living organisms. Accumulation and toxicity are under investigation.

The depth of targets is a serious problem in fluorescence measurement of living tissue. The local excitation illumination within tissue exponentially attenuates due to absorption and scattering from the surface to that depth. This problem of lack of transmission prevents us from detection in tissues deeper than 1 cm from the surface of the body at present [10]. We can detect the SN of small animals like rats, but may have difficulty in detection in larger animals because of the depth at which SNs. For example, lymph node in human is buried in fat and is located deeper than 1 cm. The detection technique to find SN up to 2 cm in depth is recommended. To solve this problem, we should select the appropriate wavelength of fluorescence and fluorescent materials, and also develop imaging techniques. Hemoglobin absorbs light in the range of visible light below 650 nm, and water absorbs light above 1,100 nm, but in the near-infrared range, between 650 and 1,100 nm, the absorption of light in living tissue is minimum. This range is called the optical window. In addition to collagen, NADH and FAD are substances that in vivo have the fluorescent wavelengths in the range of 400–500 nm. So, from this point of view, NIR range has the advantage for the fluorescence measurement. We are also investigating the application of semiconductor nanocrystal that has extremely stronger fluorescent intensity than usual fluorescent beads to increase the detection ability and fluorescence tomography based on acousto-optic modulation imaging [24].

Nanotechnology should be a great aid in improving tailor-made medicine by their hyper-sensitive and super-selective property for diagnoses. Advanced sensing technologies such as the single-molecule imaging technique and acousto-optic modulation imaging technique are also required to make the best use of the functional nanomaterials for achievement of hyper-sensitive and super-selective imaging. These novel products of advanced technologies may realize a revolution of medicine in near future.

This work was supported by Grants-in-aid for Research Projects, Promotion of Advanced Medical Technology (H14-Nano-010 and H18-Nano-001), from the Ministry of Health, Labor and Welfare, Japan.

References

1. Torchilin VP, Lukyanov AN, Gao Z, Papahadjopoulos-Sternberg B. Immunomicelles: targeted pharmaceutical carriers for poorly soluble drugs. Proc Natl Acad Sci USA. 2003;100:6039–44.
2. Krauss WC, Park JW, Kirpotin DB, Hong K, Benz CC. Emerging antibody-based HER2 (ErbB-2/neu) therapeutics. Breast Dis. 2000;11:113–24.
3. Lyons SK. Advances in imaging mouse tumour models in vivo. J Pathol. 2005;205:194–205.
4. Ishijima A, Kojima H, Funatsu T, Tokunaga M, Higuchi H, Tanaka H. Simultaneous observation of individual ATPase, mechanical events by a single myosin molecule during interaction with actin. Cell. 1998;92:161–71.
5. Wu X, Liu H, Liu J, Haley KN, Treadway JA, Larson JP. Immunofluorescent labeling of cancer marker Her2, other cellular targets with semiconductor quantum dots. Nat Biotechnol. 2003;21:41–6.
6. Gao X, Cui Y, Levenson RM, Chung LW, Nie S. In vivo cancer targeting, imaging with semiconductor quantum dots. Nat Biotechnol. 2004;22:969–76.
7. Yildiz A, Forkey JN, McKinney SA, Ha T, Goldman YE, Selvin PR. Myosin V walks hand-over-hand: single fluorophore imaging with 1.5-nm localization. Science. 2003;300:2061–5.
8. Dahan M, Levi S, Luccardini C, Rostaing P, Riveau B, Triller A. Diffusion dynamics of glycine receptors revealed by single-quantum dot tracking. Science. 2003;302:442–5.
9. Lidke DS, Nagy P, Heintzmann R, Arndt-Jovin DJ, Post JN, Grecco HE, Jares-Erijman EA, Jovin TM. Quantum dot ligands provide new insights into erbB/HER receptor-mediated signal transduction. Nat Biotechnol. 2004;22:198–203.
10. Krag DN, Weaver DL, Alex JC. Surgical resection and radiolocalization of the sentinel node in breast cancer using a gamma probe. Surg Oncol. 1993;2:335–40.
11. Tafra L, Lannin DR, Swanson MS. Multicenter trial of sentinel node biopsy for breast cancer using both technetium sulfur colloid and isosulfan blue dye. Ann Surg. 2001;233:51–9.
12. Kurebayashi J, Otsuki T, Tang CK, Kurosumi M, Yamamoto S, Tanaka K, Mochizuki M, Nakamura H, Sonoo H. Isolation and characterization of a new human breast cancer cell line, KPL-4, expressing the Erb B family receptors and interleukin-6. Br J Cancer. 1999;79:707–17.
13. Leunig M, Yuan F, Menger MD, Boucher Y, Goetz AE, Messmer K, Jain RK. Angiogenesis, microvascular architecture, microhemodynamics, and interstitial fluid pressure during early growth of human adenocarcinoma LS174T in SCID mice. Cancer Res. 1992;52:6553–60.
14. Braun RD, Abbas A, Bukhari SO, Wilson W III. Hemodynamic parameters in blood vessels in choroidal melanoma xenografts and rat choroid. Invest Ophthalmol Vis Sci. 2002;43:3045–52.
15. Carraway CA, Carvajal ME, Carraway KL. Association of the Ras to mitogen-activated protein kinase signal transduction pathway with microfilaments. Evidence for a p185 (neu)-containing cell surface signal transduction particle linking the mitogenic pathway to a membrane-microfilament association site. J Biol Chem. 1999;274:25659–67.
16. Buss F, Arden SD, Lindsay M, Luzio JP, Kendrick-Jones J. Myosin VI isoform localized to clathrin-coated vesicles with a role in clathrin-mediated endocytosis. EMBO J. 2001;20:3676–84.
17. Kamal A, Goldstein LS. Connecting vesicle transport to the cytoskeleton. Curr Opin Cell Biol. 2000;12:503–8.
18. Mross K, Niemann B, Massing U, Drevs J, Unger C, Bhamra R, Swenson CE. Pharmacokinetics of liposomal doxorubicin (TLC-D99; Myocet) in patients with solid tumors: an open-label, single-dose study. Cancer Chemother Pharmacol. 2004;54:514–24.
19. O'Brien ME, Wigler N, Inbar M, Rosso R, Grischke E, Santoro A. Reduced cardiotoxicity and comparable efficacy in a phase III trial of pegylated liposomal doxorubicin HCl (CAELYX/Doxil) versus conventional doxorubicin for first-line treatment of metastatic breast cancer. Ann Oncol. 2004;15:440–9.

20. Hamaguchi T, Matsumura Y, Nakanishi Y, Muro K, Yamada Y, Shimada Y. Antitumor effect of MCC-465, pegylated liposomal doxorubicin tagged with newly developed monoclonal antibody GAH, in colorectal cancer xenografts. Cancer Sci. 2004;95:608–13.
21. Park JW, Kirpotin DB, Hong K, Shalaby R, Shao Y, Nielsen UB. Tumor targeting using anti-her2 immunoliposomes. J Control Release. 2001;74:95–113.
22. Josephson L, Mahmood U, Wunderbaldinger P, Tang Y, Weissleder R. Pan and sentinel lymph node visualization using a near-infrared fluorescent probe. Mol Imaging. 2003;2:18–23.
23. Patrick W, Karl T, Chrstoph B. Near-infrared fluorescence imaging of lymph nodes using a new enzyme sensing activatable macromolecular optical probe. Eur Radiol. 2003;13:2206–11.
24. Kobayashi M, Mizumoto T, Shibuya Y, Takeda M, Enomoto M. Fluorescence tomography in turbid media based on acousto-optic modulation imaging. Appl Phys Lett. 2006;89:181102.

Tohoku J. Exp. Med., 2008, **216**, 47-52

Early Diagnosis of Cancer by Detecting the Chemiluminescence of Hematoporphyrins in Peripheral Blood Lymphocytes

MASAHIRO KOHNO,[1] MOTOHIRO TAKEDA,[2] YOSHIMI NIWANO,[1] RUMIKO SAITO,[1] NATSUMI EMOTO,[1] MIKA TADA,[1] TAKEMICHI KANAZAWA,[3] NORIAKI OHUCHI[2] and RIE YAMADA[4]

[1]New Industry Creation Hatchery Center, Tohoku University, Sendai, Japan
[2]Division of Surgical Oncology, Graduate School of Medicine, Tohoku University, Sendai, Japan
[3]Medical Corporation Murakami Hospital, Aomori, Japan
[4]Tohoku Electronic Industrial Co., Ltd., Sendai, Japan

Early detection and optimal treatment are the most effective means to improve cancer mortality. Mass screening for cancer has yielded a marked reduction of cancer mortality in the United States. Simple and effective methods are expected for screening of malignancy. Hematoporphyrin derivatives (HPDs) are known to accumulate in cancer cells; thus, HPD has been used for local diagnosis and photodynamic therapy of cancer. The lymphocytes of cancer patients also demonstrate the active uptake of HPD and this phenomenon has been applied for the diagnosis of cancer. In the present study, we have developed a novel method for measurement of the chemiluminescence of HPD in peripheral blood lymphocytes. HPD is composed of hematoporphyrin and its oligomers. Seven cancer patients and seven controls were recruited for this study. The primary cancers included two prostate cancers (one without metastasis and the other with lung metastasis), a renal cancer, a lung adenocarcinoma with systemic metastasis, two gallbladder cancers with lung metastasis, and a colon cancer with liver metastasis. HPD in lymphocytes was measured using a highly sensitive chemiluminescence analyzer with laser light irradiation to detect photoemission by $^1O_2$ from HPD. The intensity of chemiluminescence exhibited a linear correlation with the concentrations of HPD. In addition, the level of HPD in lymphocytes was significantly higher in cancer patients than that in healthy volunteers ($p < 0.05$). These results suggest that detection of the chemiluminescence of HPD in lymphocytes could be a sensitive and simple method for cancer diagnosis and screening. ——— Cancer; hematoporphyrin derivative; chemiluminescence analyzer; singlet oxygen; lymphocyte.
Tohoku J. Exp. Med., 2008, **216** (1), 47-52.
© 2008 Tohoku University Medical Press

Photodynamic therapy involves the selective uptake and retention of photosensitizing agents for the diagnosis and treatment of malignancies (Lipson et al. 1961; Cortese et al. 1979; Hayata et al. 1982). The accumulation of photosensitizing agents and their activation by a specific wavelength of light (Dougherty et al. 1975; Gomer et al. 1979; Dougherty 1987) lead to the formation

Received February 29, 2008; revision accepted for publication July 15, 2008.
Correspondence: Masahiro Kohno, Ph.D. New Industry Creation Hatchery Center, Tohoku University, Aoba 6-6-10, Aramaki, Aoba-ku, Sendai, 980-8579, Japan.
e-mail: mkohno@niche.tohoku.ac.jp

of an excited triplet state and chain reactions of reactive oxygen species (ROS); singlet oxygen ($^1O_2$), superoxide (O_2^-), hydrogen peroxide (H_2O_2) and hydroxyl radical (HO˙) can selectively target tumor tissues (Peterson et al. 1981; Pótó et al. 1989; Ando et al. 1997). Therefore, measuring the uptake of hematoporphyrin derivative (HPD) in cancerous tissue has been applied to the diagnosis of cancer. Up to now, among the potential activities of HPD for various types of cells, the interaction between peripheral blood lymphocytes and HPD has been also intensively investigated. Its clinical application for screening and follow-up after cancer therapy has been attempted by measuring the electron spin resonance (ESR) and fluorescence spectrum. Previous studies have attempted to measure the uptake of HPD by fluorescence for cancer screening and follow-up after cancer therapy. However, the nonspecific fluorescence of peripheral blood lymphocytes and insufficient sensitivity of photo-detectors prevented the detection of small amounts of HPD in lymphocytes (Itabashi et al. 1984; Docchio et al. 1984; He et al. 1989; Tanielian et al. 2001).

Recent refinements in photo-detectors and measurement methods enabled the detection of very small amounts of HPD (< 10 μg/ml). The fluorescence detection system was composed of a highly sensitive photon counting system and a laser. The amount of HPD is measured by the light intensity as photon counts from $^1O_2$ generated from HPD by laser irradiation.

Cancer is a major cause of mortality. Early detection and proper treatment are the most effective means to reduce cancer mortality. Mass screening is essential to identify cancer patients in early stages. Although mass screenings have markedly reduced cancer mortality in the United States, they are expensive and require extensive effort and time. Therefore simple and cost-effective methods are required for cancer screening, as well as for diagnosis and treatment.

In this report, we examined the uptake of HPD by peripheral blood lymphocytes of cancer patients and healthy volunteers by using a novel method for measurement of the chemiluminescence of HPD.

Materials and Methods

Chemicals

Hematoporphyrin (HP) was purchased from Sigma Chemical Company (St. Louis, MO, USA) and HPD was purchased from Seikagaku Kogyo Co., Ltd. (Tokyo, Japan). The elements of HPD were HP and its oligomers. The average molecular mass of HPD was about 3,000 Da. HPD was diluted in saline to be a concentration of 150 mg/30 ml. The final concentration of HPD was about 1.66 mM. HP was prepared in saline at a concentration of 5 mM. Ficoll-Paque PLUS was purchased from GE Healthcare Biosciences AB (Uppsala, Sweden).

Participants

Seven healthy volunteers and seven cancer patients were recruited at Tohoku University Hospital and Medical Corporation Murakami Hospital (Aomori, Japan). All of the participants were carefully questioned to determine whether they had any malignancies or inflammatory diseases. The primary cancer patient group included two prostate cancers (one was negative for metastasis and the other was positive for lung metastasis), a renal cancer with anemia, a lung adenocarcinoma with systemic metastasis, two gallbladder cancers with lung metastasis and a colon cancer with liver metastasis.

Isolation of lymphocytes

Lymphocytes were isolated from the venous blood by density gradient centrifugation on Ficoll-Paque PLUS. Isolated lymphocytes were diluted to 5×10^6 cells/ml with saline. For HPD-staining, 1×10^6 lymphocytes were treated with 100 μl of 1.66 mM HPD solution for 10 min at 37°C. Then the lymphocytes were washed twice in phosphate-buffered saline (PBS) and resuspended in 100 μl of saline. Fifty μl of the suspension of lymphocytes stained with HPD was used for the chemiluminescence (CL) measurements.

Measurement setup and analytical procedures

The detection of CL was performed using a chemiluminescence analyzer (CLA) (MLA-GOLDS; Tohoku Electronic Industrial Co., Ltd., Sendai, Japan) which consisted of a photomultiplier tube (R550P, Hamamatsu Photonics, Shizuoka, Japan), a semiconductor laser (VIOLET LASER DIODE: NDHV310APC; Nichia Corporation, Tokushima, Japan) with a wavelength at 408 nm and a long pass filter of 600 nm. To minimize cell damage, the output energy of the laser was controlled at 10 mW.

The intensity of the CL of lymphocytes was measured for lymphocytes with HPD and lymphocytes without HPD under laser irradiation at 408 nm. The intensity of the CL of HPD in the lymphocytes was assessed by subtracting the CL of lymphocytes without HPD from the CL of those with HPD. Each assay was performed in duplicate.

Statistical analysis

The significance of the difference between cancer patients and healthy volunteers was assessed by Student's *t*-test and values of $P < 0.05$ were considered to be significant.

This study was approved by the Ethics Committee of Tohoku University.

Results

The representative emission spectra observed in lymphocytes of a colon cancer patient with and without HPD staining are shown in Fig. 1. The emission spectrum of HPD in lymphocyte of cancer patients exhibited two peaks at 560~580 nm and 620~640 nm. One of these peaks at 620~640 nm was not observed in the lymphocytes of cancer patients without HPD. This is consistent with the previous finding that emission in the range of 620~640 nm is caused by $^1O_2$.

The CL intensity of HP was measured at several concentrations to make a calibration curve and to determine the detection limit of HPD in lymphocytes. The CL intensities in the range over 600 nm showed a strong positive correlation with the HP concentrations (Fig. 2). The correlation coefficient was 0.9951. Since the specific molecular structure, mass and composition of the HPD is unclear, a calibration curve of CL of single HP was used to determine the concentration of the HPD. The detection limit of the CLA for HPD was determined to be lower than 1 pmol (Fig. 2B). The sensitivity of the CLA was 1000-fold higher than that of the commercially available fluorescence spectrometry.

Fig. 3 shows the intensity of CL from the lymphocytes of cancer patients and of healthy volunteers. A nonspecific CL of 5,000-7,000 cps was observed in the lymphocytes of all participants without HPD. Therefore, the specific CL of $^1O_2$ was calculated by subtraction of the CL without HPD from the CL with HPD (Fig. 4). The average HPD concentration in the lymphocytes of cancer patients was estimated to be 100 pmol in 1.25×10^5 cells using the calibration curve (Fig. 2). The CL intensity from the lymphocytes of cancer patients was significantly higher than that of the lymphocytes from healthy volunteers (Fig. 3, $p < 0.05$).

Discussion

A significant uptake of HPD was observed in

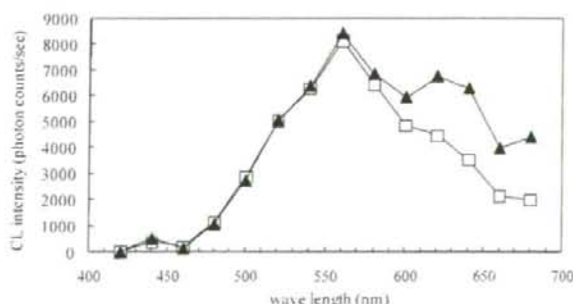

Fig. 1. Fluorescence spectra of the lymphocytes of a colon cancer.
▲: Fluorescence with HPD staining
□: Fluorescence without HPD staining
The line with □ indicates the fluorescence spectrum of the lymphocytes from a colon cancer without HPD. The line with ▲ indicates the fluorescence spectrum of the lymphocytes from a colon cancer with HPD.

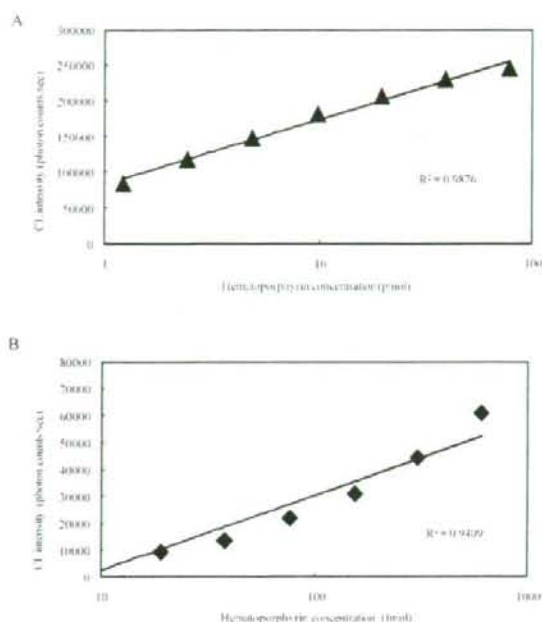

Fig. 2. Calibration curve of the standard HP concentration and chemiluminescence intensity.
A. Correlation between the fluorescence intensity and HP in the high concentration range (1 to 100 pmol).
B. Correlation between the fluorescence intensity and HP in the low concentration range (10 to 1,000 fmol).

the peripheral blood lymphocytes of all cancer patients by subtraction of the emission intensity from that before the treatment with HPD. In contrast, there was no significant difference between the emission intensity before and after the treatment with HPD in normal volunteers. These results suggest that the selective uptake of HPD by lymphocytes can be applied for the diagnosis and screening of cancer.

Fluorescence measurements have been used for the diagnosis of various diseases (Kinoshita et al. 1988). In particular, the measurement of ultra weak photon emission has been used to study the biological activity of leukocytes and to find biomarkers in whole blood that are related to aging (Inaba et al. 1979; Dodeigne et al. 2000). The fluorescence measurement of peripheral blood lymphocytes stained with HPD has not been used for clinical applications because of the nonspecific fluorescence of lymphocytes and poor sensitivity of existing florescence spectrometers (Itabashi et al. 1984; Docchio et al. 1984; He et al. 1989; Tanielian et al. 2001). It was possible to discriminate the luminescence of $^1O_2$ from the nonspecific CL of lymphocytes by measuring the CL within the range of 620~640 nm with a highly sensitive CLA system.

Although the precise mechanism controlling the selective uptake of HPD in lymphocytes of cancer patients is still unknown, HPD has been reported to accumulate in the hydrophobic region of B cells and NK cells but not T cells (Kessel et al. 1983; Berki et al. 1998; Savitskii, et al. 2004). Therefore, it has been hypothesized that populations of cells with a high affinity to HPD, such as B cells and NK cells, may show a relative increase among the lymphocytes in cancer patients. The lymphocyte profile should therefore

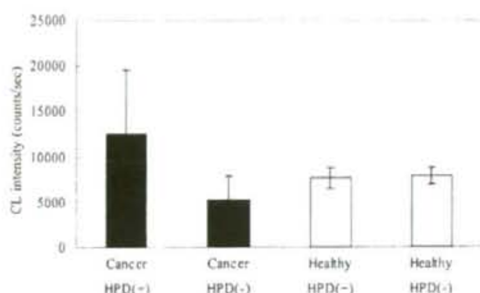

Fig. 3. Intensity of chemiluminescence from lymphocytes of cancer patients and of healthy volunteers.
+: Fluorescence with HPD staining
−: Fluorescence without HPD staining
The black columns indicate the CL intensity of the lymphocytes from cancer patients with and without positive staining for HPD ($n = 7$). The white columns indicate the chemiluminescence of lymphocytes from healthy volunteers with and without positive staining for HPD ($n = 7$).

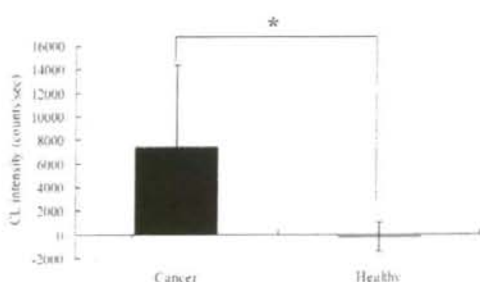

Fig. 4. Chemiluminescence from lymphocytes of cancer patients and of healthy volunteers.
The CL intensity of HPD was calculated by subtraction of the CL without HPD from the CL with HPD for each participant.
*: Statistical significance between cancer patients and healthy volunteers ($p < 0.05$).

be examined as a next step.

In this study, a high uptake of HPD was observed in some types of malignancies. The results suggest that this novel method could be used for mass screening as a simple and cost-effective method to detect malignancies.

This method could also serve as an adjunct to non-invasive diagnosis by positron emission tomography, magnet resonance imaging system or X-ray CT.

References

Ando, T., Yoshikawa, T., Tanigawa, T., Kohno, M., Yoshida, N. & Kondo, M. (1997) Quantification of singlet oxygen from hematoporphyrin derivative by electron spin resonance. *Life Sci.*, **61**, 1953-1959.

Berki, T. & Németh, P. (1998) Novel method for in vitro depletion of T cells by monoclonal antibody- targeted photosensitization. *J. Immunol. Methods*, **211**, 139-146.

Cortese, D.A., Kinsey, J.H., Woolner, L.B., Payne, W.S., Sanderson, D.R. & Fontana, R.S. (1979) Clinical application of a new endoscopic technique for detection of in situ bronchial carcinoma. *Mayo Clin. Proc.*, **54**, 635-641.

Docchio, F., Ramponi, R., Sacchi, C.A., Bottiroli, G. & Freitas, I. (1984) Time-resolved fluorescence spectroscopy of hematoporphyrin-derivative in human lymphocytes. *Chem. Biol. Interact.*, **50**, 135-141.

Dodeigne, C., Thunus, L. & Lejeune, R. (2000) Chemiluminescence as diagnostic tool. A review. *Talanta*, **51**, 415-439.

Dougherty, T.J. (1987) Photosensitizers: Therapy and detection of malignant tumors. *Photochem. Photobiol.*, **45**, 879-889.

Dougherty, T.J., Grindey, G.B., File, R., Weishaupt, K.R. & Boyle, D.G. (1975) Photoradiation therapy. II. Cure of animal tumors with hematoporphyrin and light. *J. Natl. Cancer Inst.*, **55**, 115-121.

Gomer, C.J. & Dougherty, T.J. (1979) Determination of [^{3}H]- and [^{14}C]hematoporphyrin derivative distribution in malignant and normal tissue. *Cancer Res.*, **39**, 146-151.

Hayata, Y., Kato, H., Ono, J., Matsushima, Y., Hayashi, N., Saito, T. & Kawate, N. (1982) Fluorescence fiberoptic bronchoscopy in the diagnosis of early stage lung cancer. *Recent Results Cancer Res.*, **82**, 121-130.

He, D., Soter, N.A. & Lim, H.W. (1989) The late phase of hematoporphyrin derivative- induced phototoxicity in mice: release of histamine and histologic changes. *Photochem. Photobiol.*, **50**, 91-95.

Inaba, H., Shimizu, Y., Tsuji, Y. & Yamagishi, A. (1979) Photon counting spectral analyzing system of extra-weak, chemi- and bioluminescence for biological applications. *Photochem. Photobiol.*, **30**, 169-175.

Itabashi, M., Aoyama, M., Kohno, M. & Tanaka, N. (1984) ESR (electron spin resonance) analysis of cancer patient lymphocytes stained with hematoporphyrin D. *Gan No Rinsho*, **30**, 1293-1298.

Kessel, D. & Chou, T.H. (1983) Tumor-localizing components of the porphyrin preparation hematoporphyrin derivative. *Cancer Res.*, **43**, 1994-1999.

Kinoshita, S., Seki, T., Liu, T.F. & Kucida, T. (1988) Fluorescence of hematoporphyrin in living cell and in solution. *J. Photochem. Photobiol. B: Biol.*, **2**, 195-208.

Lipson, R.L., Baldes, E.J. & Olson, A.M. (1961) The use of a derivative of hematoporphyrin in tumor detection. *J. Natl. Cancer Inst.*, **26**, 1-11.

Peterson, D.A., Mckelvey, S. & Edmondson, P.R. (1981) A hypothesis for the molecular mechanism of tumor killing by porphyrins and light. *Med. Hyphotheses*, **7**, 201-205.

Pótó, L. & Berki, T. (1989) Investigation on the free radical producing effect of hematoporphyrin (a spin trapping study). *Acta Physiol. Hung.*, **74**, 285-290.

Savitskii, V.P., Zorin, V.P., Potapnev, M.P. & Potapenko, A.Y. (2004) Comparative analysis of accumulation of chlorine

e6 and hematoporphyrin derivatives in subpopulations of peripheral blood lymphocytes. *Bull. Exp. Biol. Med.*, **138**, 158-162.

Tanielian, C., Schweitzer, C., Mechin, R. & Wolff, C. (2001) Quantum yield of singlet oxygen production by monomeric and aggregated forms of hematoporphyrin derivative. *Free Radic. Biol. Med.*, **30**, 208-212.

Materials Transactions
Special Issue on Advances in Computational Materials Science and Engineering V
© 2008 The Japan Institute of Metals

TD-DFT Studies on Hematoporphyrin and Its Dimers

A. Suvitha[1,*], R. V. Belosludov[1], H. Mizuseki[1], Y. Kawazoe[1],
M. Takeda[2], M. Kohno[2] and N. Ohuchi[3]

[1] *Institute for Materials Research, Tohoku University, Sendai 980-8577, Japan*
[2] *NICHe, Tohoku University, Sendai 980-8579, Japan*
[3] *Department of Surgical Oncology, Tohoku University School of Medicine, Sendai 980-8579, Japan*

A theoretical study has been performed on a hematoporphyrin and its dimers which are components of Photofrin, a photosensitizer. Full geometry optimizations have been carried out using the PBEPBE functional and 6-31G(d) basis set. This combination gives better agreement with X-ray crystal data of porphyrin. Among the dimers studied, the C–C linked structure is found to have the highest stability. The predicted change of free energy ($\Delta G = -13.9$ kcal/mol) suggests that the interconversion of ester to ether would be thermodynamically favorable. The time-dependent density functional theory (TDDFT) studies show that Q-band absorption maxima undergo a less intense transition and low oscillator strength, indicating that dimers have activity when treated under higher dosage. [doi:10.2320/matertrans.MB200829]

(Received June 2, 2008; Accepted July 22, 2008; Published September 3, 2008)

Keywords: *hematoporphyrin, time-dependent density functional theory (TDDFT), photodynamic therapy, spectroscopy*

1. Introduction

Photodynamic therapy (PDT) is a non-invasive medical technique for the treatment of various types of diseases in oncology and ophthalmology.[1–4] The basic principle of PDT for cancer is the combination of a photosensitizing drug capable of absorbing within the body's therapeutic window ($\lambda = 620$–850 nm), a light source (*e.g.*, a laser) of an appropriate wavelength and molecular oxygen. The photosensitizer, which accumulates preferentially in cancer cells and has a low dark toxicity, is injected into human body tissue and then irradiated with visible light. After irradiation, the light-activated molecule undergoes different reactions and can decay from a singlet to a triplet excited state through a radiationless transition (intersystem crossing). The rate of the latter step is enhanced by the presence of an atom with a high atomic number (heavy-atom effect) in the molecule. The key cytotoxic agent is singlet molecular oxygen $^1O_2$, which is generated by an energy-transfer reaction from the photosensitizer triplet state to the ground state molecular oxygen $^3O_2$.[5] For an efficient process, the photosensitizer's triplet-state energy should match the first excitation energy of molecular oxygen (0.98 eV).

The photosensitizers for cancer treatment currently approved for clinical use belong to various groups of photofrin, which is a complex mixture of non-metallic oligomeric porphyrins (Hematoporphyrins).[6,7] The mixture is believed to contain two to nine porphyrin units of oligomeric and dehydrated products that are linked by ether, ester or a C–C linkage (Scheme 1).[8] The lack of available experimental techniques, to isolate and purify the higher oligomers is a big challenge till to date.[9] There are several structure-activity relationship studies on hematoporphyrin and their distribution and photodynamic activity but none of these descriptive studies are quantitative and hence could be used to predict the exact structural information of the compound that are responsible for PDT activity.[10]

In recent years, the Time-Dependent Density Functional theory (TDDFT) has proved its efficiency in the evaluation of electronic spectra and could predict the vertical excitation energies and oscillator strength with low computational cost effect.[11,12] In this paper, we have undertaken systematic study on the structural, energetic and spectroscopic behaviour for monomer and dimer a component of a classical photosensitizer, photofrin that are used in PDT. The theoretical work presented here is closely tied to experimental work, where to investigate the effect of type of linkage on absorption spectral behaviour of monomer and dimers, as higher oligomer will have very complex spectra that may be hard to understand. In particular, we have determined: (i) the structures and geometric conformation; (ii) the absorption spectra and their electronic origin; (iii) the singlet–triplet energy gap for the monomer and dimers with DFT and TD-DFT methods. Moreover, we have compared them with available experimental data, in order to get a clear insight into the nature of molecule responsible for PDT activity.

2. Computational Methods

All calculations were carried out by using the Gaussian 03 package.[13] Full geometrical optimizations, frequency calculations and TD-DFT studies has been carried out employing the PBEPBE functional, based on the generalized gradient functional proposed by Perdew, Burke and Ernzerhof (PBE) with standard 6-31G(d) basis set. Recent results has revealed the choice of 6-31G(d) as basis set, was found to predict the molecular geometry and vertical excitation more precisely.[14] No symmetry constraints were imposed during the geometry optimizations. In all cases, frequency calculations were done on optimized structures to confirm the local minima. Restricted formalism was applied for the singlet electronic states and unrestricted formalism for the triplet states. Absorption spectra were computed as vertical electronic excitation energy from the minima of the ground-state structures by using time-dependent density functional response theory.

*Corresponding author, E-mail: suvita@imr.edu

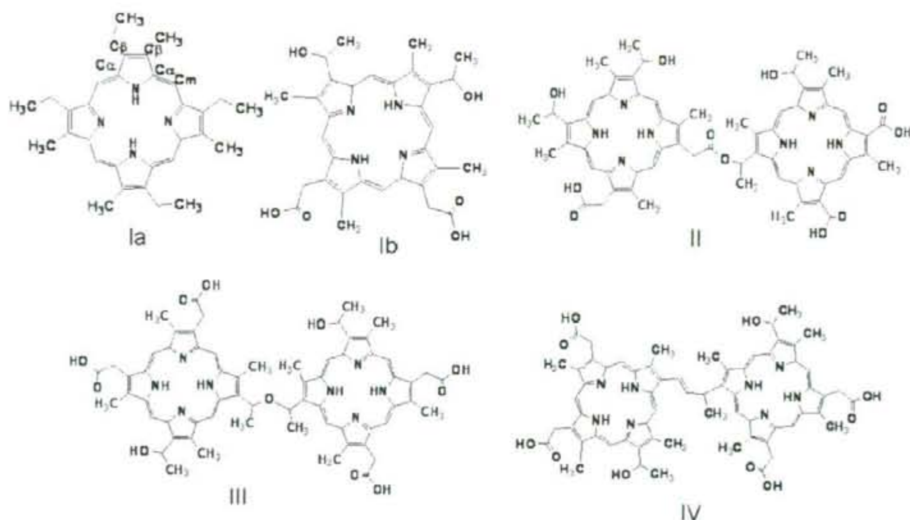

Fig. 1 (Ia) Porphyrin (Ib) Hematoporphyrin (II) Ester linked dimer (III) Ether linked dimer and (IV) C-C linked dimer.

Table 1 Experimental and calculated bond distances (Å) at various theory levels.

Bond label	HF	B3LYP	B3P86	PBEPBE	Expt.*
C-Cαm	1.351	1.396	1.384	1.407	1.405
C-Cαβa	1.393	1.446	1.446	1.474	1.457
C-Cαβc	1.481	1.442	1.444	1.446	1.430
C-Cββa	1.343	1.387	1.380	1.396	1.359
C-Cββc	1.406	1.382	1.380	1.392	1.349
Cα-NH	1.360	1.367	1.372	1.377	1.379
Cα-N	1.386	1.361	1.372	1.372	1.370

*See Reference 15)

3. Results and Discussion

3.1 Molecular geometries

Hematoporphyrin monomer can undergo oligomerization under various pH conditions to form three different possible linkages. Experimentally, known dimers are ether(-C-O-C-) linked, ester(-CO-O-C-) linked and -C-C- linked hematoporphyrins [Fig. 1].[15] Since hematoporphyrin derivatives are difficult to isolate in its pure state, no single crystal data are available and hence comparison has been made with the analogues porphyrin system. Moreover, porphyrin and hematoporphyrin have similar electronic-structure based properties.[16] Monomer of hematoporphyrin has been optimized at the different theory levels such as HF, B3LYP, B3P86 and PBEPBE with basis set of 6-31G(d) in the gas phase. Previous results has show the choice of 6-31G(d) as basis set, was able to predict the molecular geometry and vertical excitation more precisely on porphyrin system.[14] Table 1 shows the selected bond lengths obtained under various theory levels. Among the methods tested, PBEPBE has better agreement with experimental values of the porphyrin system. Therefore, we have used PBEPBE method with 6-31G(d) basis set for optimizing the dimer structures.

To identify the most stable conformer for the dimers, optimizations were carried out with different initial geometries such as, the one in which two porphyrin units are in-plane and the other in which they are in perpendicular to each other. The fully optimized conformers with the lowest energy are shown in Fig. 2. The structures shows that the C–C linked isomer have a partial linear structure, while the other two isomers have a folded structure. In addition to the folding observed between the two porphyrin rings effective π-π interactions between the two porphyrin rings were observed in the case of ether. Among the dimers studied, the C–C linked structure has been found have the highest stabilization energy and between the ether and ester isomers, ether was found to be 13.3 kcal/mol more stable than ester isomer. The predicted free energy change ($\Delta G = -13.9$ kcal/mol) suggests that the interconversation of ether to ester would be thermodynamically favorable at room temperature, which has already been observed experimentally in aqueous alkaline media.[17] Moreover, the frequency calculations have been performed for most stable configurations of three types linked isomers. These calculations reveal that all of Eigen values of Hessian matrix are positive, and hence, the corresponding frequencies are real. This means that these structures are indeed (at least local) minima.

3.2 Electronic spectra of monomer and dimer

Absorption spectra of monomer and dimers of hematoporphyrin were computed using TDDFT studies and results are provided in Table 2. The computed λ_{max} value for the monomer agrees well with experimental data. As their exist highly conjugated ring, these porphyrin-like systems show intense absorption bands around 400 nm, which is called as B-band region, followed by weaker satellites peaks between 500 to 800 nm, known as the Q-band region. We have computed spin-allowed singlet transitions for the compounds in vacuum and their relative results are reported in Table 2.

Table 2 Comparison of UV-Vis data and TD-DFT values.

Compounds	B-band	Q-bands			
Monomer	397.0 **(396.0)***	505.0 **(505.0)**	538.0 **(537.0)**	566.6 **(567.0)**	617.2 **(617.0)**
Ester linked dimer	398.4	507.2	532.8	568.0	622.4
Ether linked dimer	399.2 **(398.0)**	505.6 **(503.0)**	533.6 **(535.0)**	570.0 **(570.0)**	623.2 **(624.0)**
C-C linked dimer	399.2	505.6	533.6	567.2	623.2

*Experimental values of wavelength in nm are given in parenthesis.

Table 4 Total energies and singlet–triplet energy gaps (ΔE) for the studied dimers.

Compounds	Electronic states	Total energy (Hatrees)	ΔE (eV)
Ether linked dimer	^1A	−3896.74138971	0.00
	^3A	−3896.68414099	1.56
Ester linked dimer	^1A	−3896.7171993	0.00
	^3A	−3896.6562231	1.69
C-C linked dimer	^1A	−3824.60693816	0.00
	^3A	−3824.55089916	1.52

Table 3 Excitation energies (ΔE) in eV for peak around 620 nm of Q band with orbitals contributions.

Molecule	Symmetry	Excitation energy ΔE [eV]	Oscillator strength	Transition character*
Ether linked	A_{1u}	2.04	0.0001	HOMO-2 → LUMO (63.6%) HOMO-2 → LUMO+2 (3.8%) HOMO-3 → LUMO+3 (2.3%)
C-C linked	A_{1u}	2.02	0.0072	HOMO-1 → LUMO+2 (34.6%) HOMO-1 → LUMO+4 (49.7%)
Ester linked	A_{1u}	2.07	0.0002	HOMO-2 → LUMO (19.4%) HOMO-2 → LUMO+3 (24.3%)

*The percentage contribution of orbitals to the transition are given in parenthesis.

The oscillator strengths and the transition character along with the percentage contribution of orbitals to the transition in parenthesis for peak around 620 nm are provided in Table 3.

The lowest excitation energy in the wavelength region of 620 nm in dimers gives rise to the weaker transition, with oscillator strength varying from 0.0072 to 0.00001. This transition stems mainly from the HOMO-2–LUMO+3 excitation and HOMO-2 to LUMO for the ester linked dimer. While three transitions HOMO-2–LUMO, HOMO-3–LUMO+3 and HOMO-2 to the LUMO+2 are responsible for the transition in the case of the ether linked dimer. In the case of C–C linked dimer there is a contribution from the HOMO-1–LUMO+2 and HOMO-1–LUMO+4. The oscillator strength of C–C linked dimer is 100 times higher than other type of linkages shows that C–C linked type can have better PDT. This lowest excitation energy varying between 2.02–2.07 eV corresponds to the band, which plays a basic role in PDT applications. There is no extensive π–conjugation between the two hematoporphyrin units in all dimers and hence no significant shift in the excitation energy has been observed. Moreover, as there is no change in the number of π-electrons in the porphyrin core, which contributes to the increase and shift in absorbance maxima in the case of porphyrin, chlorin, and bacteriochlorin.[18]

3.3 Singlet–triplet energy difference

One of the basic requisites of a photosensitizer for achieving an optimal performance in PDT is represented by its singlet–triplet energy gap (greater than or equal to 0.98 eV).[19] The singlet–triplet energy gaps (ΔE) for the dimers are reported in Table 4. The series has ΔE values ranging from 1.52 eV to 1.69 eV, where values higher than 0.98 eV are found. Thus the series should induce the triplet–singlet molecular-oxygen transitions. However, it is worth noting that, owing to the small difference in ΔE values, this has to be approached with caution.

4. Summary and Conclusion

In conclusion we studied the ground-state geometries and electronic absorption spectra of hematoporphyrin and its dimers using TD-DFT approach. The PBEPBE functional along with the all electron 6-31G(d) basis set was found to give better results, indicating that the possibility of employing the same functional with basis set for higher oligomers. Dimers of different possible linkages have been optimized and they shows that the C–C linked isomer have a partial linear structure, while the other two isomers have a folded structure. The inter-conversion of ester- to ether-linked dimer is thermodynamically favoured process, which agrees well the experimental observation. Owing to their use in photo-

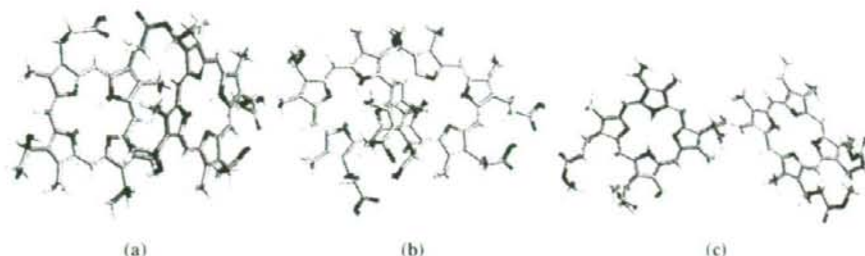

Fig. 2 Optimized structures of: (a) Ester linked; (b) Ether linked; and (c) the C-C linked dimers.

dynamic therapy, particular attention was devoted to two spectral aspects that are important for an ideal photosensitizer: (1) determination of the energetic gap between singlet and triplet excited states, shows that the values are greater than 0.98 eV and (2) computation of the Q-band absorption maximum shows that they have weaker transitions with low oscillator strength. Among the dimers C–C linked dimer has higher oscillator strength. Thus dimers may involve in the PDT activity, when used at higher dosage.

Acknowledgement

Grant support: Grants-in-aid for Research Project: Promotion of Advanced Medical Technology (H18-Nano-001); Ministry of Health, Labour and Welfare of Japan is gratefully acknowledged. R.V.B. thanks the Ministry of Education, Culture, Sports, Science and Technology of Japan (Grant No. 17686072) for financial support. The authors are also grateful to the staff of CCMS, IMR, and Tohoku University for computational support.

REFERENCES

1) I. J. MacDonald and T. J. Dougherty: J. Porphyrins Phthalocyanines 5 (2001) 105–129.
2) Y. Van Tenten, H. J. Schuitmaker, A. De Wolf, B. Willekens, G. F. J. M. Vrensen and M. J. Tassignon: Exp. Eye Res. 72 (2001) 41–48.
3) T. J. Dougherty, C. J. Gomer, B. W. Henderson, G. Jori, D. Kessel, M. Korbelik, J. Moan and Q. Peng: J. Natl. Cancer Inst. **90** (1998) 889–905.
4) C. Avendano and J. Carlos Menendez: *Medicinal chemistry of anticancer drugs* (Elsevier's Science & Technology Rights, Department in Oxford, UK, 2008) pp. 93–132.
5) R. Bonnett: Chem. Soc. Rev. **24** (1995) 19–33.
6) R. K. Pandey and G. Zheng: *Porphyrins as Photosensitizers in Photodynamic Therapy*, vol. 6. (Academic Press: San Diego, 2000).
7) M. R. Detty, S. L. Gibson and S. J. Wagner: J. Med. Chem. **47** (2004) 3897–3915.
8) M. M. Siegel, K. Tabei and R. Tsao: J. Mass Spectrom. **34** (1999) 661–669.
9) K. M. Kadish, K. M. Smith and R. Guilard: *The Prophyrin Handbook* (Academic New York, 1978) pp. 189–190.
10) B. W. Henderson, D. A. Bellnier, W. R. Greco, A. Sharma, R. K. Pandey, L. A. Vaughan, K. R. Weishaupt and T. J. Dougherty: Cancer Res. **57** (1997) 4000–4007.
11) R. J. Deeth: Faraday Discuss. **124** (2003) 379–391.
12) V. N. Nemykin, R. G. Hadt, R. V. Belosludov, H. Mizuseki and Y. Kawazoe: J. Phys. Chem. A **111** (2007) 12901–12913.
13) Gaussian 03, Revision C.02, M. J. Frisch, *et al.* Gaussian, Inc., Wallingford 2003.
14) K. A. Nguyen and R. Pachater: J. Chem. Phys. **114** (2001) 10757–10767.
15) C. J. Byrne, L. M. Marshallsay and A. D. Ward: J. Photochem. Photobiol. **6** (1990) 13–27.
16) C. J. Byrne, M. A. Cooper, P. A. Cowled, R. A. W. Johnstone, L. Mackenzle, L. V. Marshallsay, I. K. Morris, C. A. Muldoon, M. J. Raftery, S. S. Yin and A. D. Ward: Aust. J. Chem. **57** (2004) 1091–1102.
17) C. J. Byrne and A. D. Ward: Aust. J. Chem. **44** (1991) 411–426.
18) R. K. Pandey, J. F. Majchrzycki, K. M. Smith and T. J. Dougherty: Proc. SPIE **1065** (1989) 164–174.
19) N. J. Turro: *Singlet oxygen and chemiluminescent organic reactions, Modern Molecular Photochemistry*, (University Science Books: California, 1991) pp. 583–593.

EXPERIMENTAL CELL RESEARCH 314 (2008) 3563–3569

available at www.sciencedirect.com

ScienceDirect

www.elsevier.com/locate/yexcr

Research Article

Intracellular imaging of targeted proteins labeled with quantum dots

Jungwoo Yoo[a,1], *Taketoshi Kambara*[b,2], *Kohsuke Gonda*[b,3], *Hideo Higuchi*[b,2,*]

[a]*Department of Material Science, Graduate School of Engineering, Tohoku University, Sendai, Japan*
[b]*Biomedical and Engineering Research Organization, Tohoku University, Sendai, Japan*

ARTICLE INFORMATION

Article Chronology:
Received 17 July 2008
Revised version received
5 September 2008
Accepted 7 September 2008
Available online 26 September 2008

Keywords:
Motor protein
Actin
Microtubule
Kinesin
Quantum dots
Microscope
Imaging

ABSTRACT

We developed a new method for imaging the movement of targeted proteins in living cancer cells with photostable and bright quantum dots (QDs). QDs were conjugated with various molecules and proteins, such as phalloidin, anti-tubulin antibody and kinesin. These bioconjugated QDs were mixed with a transfection reagent and successfully internalized into living cells. The movements of individual QDs were tracked for long periods of time. Phalloidin conjugated QDs bound to actin filaments and showed almost no movement. In contrast, anti-tubulin antibody conjugated QDs bound to microtubules and revealed dynamic movement of microtubules. Kinesin showed an interesting behavior whereby kinesin came to be almost paused briefly for a few seconds and then moved once again. This is in direct contrast to the smoothly continuous movement of kinesin in an *in vitro* assay. The maximum velocity of kinesin in cells was faster than that in the *in vitro* assay. These results suggest that intracellular movement of kinesin is different from that in the *in vitro* assay. This newly described method will be a powerful tool for investigating the functions of proteins in living cells.

© 2008 Elsevier Inc. All rights reserved.

Introduction

Recent development of imaging techniques for single molecules provides detailed information of the molecular mechanism of proteins [1–4]. However, the mechanism underlying the function of these molecules within the cells is still not known. Many studies of cell biology are utilizing organic fluorophores and fluorescence proteins, such as Cy3 and GFP, as probes to visualize single protein molecules, and have been very successful [5,6]. Single molecule observation of these fluorophores, however, is available only for short periods of a few seconds due to their rapid photo bleaching. Thus, development of a new technique to image single molecules of targeted proteins for long periods of time is crucial in order to investigate the detailed mechanisms of the proteins in living cells. The bright and photostable quantum dots (QDs) are useful for detecting the behavior of biomolecules in living cells for long periods of time [7–11], 1 h or longer [10]. The positions of bright fluorescence spots were determined with more than one nanometer accuracy for the long periods, when the QDs are excited with very bright light [12,13]. Thus, the direct labeling of biomolecules in a living cell with QDs is important for the future advances of biological and medical research [12,14,15].

* *Corresponding author.* Department of Physics, Graduate School of Science, University of Tokyo, Hongo Bunkyo-ku Tokyo, Japan 113-8654. Fax: +81 35841 7646.
E-mail address: higuchi@phys.s.u-tokyo.ac.jp (H. Higuchi).
[1] Institute of Multidisciplinary Research for Advanced Materials, Tohoku University, 2-1-1, Katahira, Aoba-ku, Sendai 980-8577, Japan.
[2] Department of Physics, Graduate School of Science, the University of Tokyo, Hongo Bunkyou-ku Tokyo 113-8654, Japan.
[3] Department of Nano-Medical Science, Graduate School of Medicine, Tohoku University, Seiryo-machi, Aoba-ku, Sendai 980-8574, Japan.

0014-4827/$ – see front matter © 2008 Elsevier Inc. All rights reserved.
doi:10.1016/j.yexcr.2008.09.014

Internalization of the QD-bioconjugates across the cell membrane into cytoplasm of living cells is very challenging for intracellular imaging. Several methods for the internalization of QD-bioconjugates have been tested, electroporation [16], liposome fusion [17,18], microinjection [17] and cell penetrating polymers and peptides [19,20]. These methods, however, could internalize QDs in aggregates [17,18]. To image single molecules labeled with QDs in living cells, the bioconjugated QDs need to be delivered in a monodispersion and have increased targeting efficiency. Recently, osmotic lysis of pinosomes was used for QD internalization [21]. This method is simple but has sometimes resulted in damage of cellular functions [22].

Our method using the lipid transfection has been widely used for DNA transfection in cell biology [23] to deliver QDs into cells without damaging cellular functions. We successfully delivered the bioconjugated QDs and imaged them internally using QDs conjugated with phalloidin, anti-tubulin antibody and kinesin as excellent examples of small molecule, antibody and enzyme, respectively (Fig. 1). Here, the interesting dynamics of microtubule and the intracellular-specific behavior of kinesin were discovered for the first time. Therefore, the methods in the present study will be a powerful tool to image other cellular components as well as motor proteins using photostable QDs as a probe.

Materials and methods

Preparation of phalloidin–QD-bioconjugate

For the specific labeling of actin filaments, phalloidin molecules were conjugated to QDs. Amino functionalized PEG coated QDs 655 (Qdot® nanocrystals, Invitrogen Co.), where the number indicates the emission wavelength, were cross-linked to amino functionalized phalloidin (Amino Phalloidin, Alexis Biochemicals) by Bis (sulfosuccinimidly) suberate (BS3, Pierce Chemicals). BS3 is a homobifunctional *N*-hydroxysuccinimide ester (NHS ester) that reacts efficiently with primary amino groups. The procedure to make phalloidin conjugated QDs is described as follows: 0.03 mg of BS3 was added to 50 µl of 4 µM QD solution and incubated for 30 min at room temperature (~25 °C). Excess cross-linker was removed by NAP-5 column (Amersham Biosciences) with PBS (pH 7.4). 6 µg of amino-phalloidin was then added to the solution, and incubated for 2 h with gently mixing at room temperature. To remove the free phalloidin, a 100 kDa ultrafiltration filter (Nanosep, Pall Life Sciences) was used according to manufacturer instructions. The phalloidin–QDs were resuspended in phosphate buffered saline, PBS (pH 7.4) and stored at 4 °C. The final concentration of phalloidin–QDs was determined by measuring the absorbance of the conjugate solution.

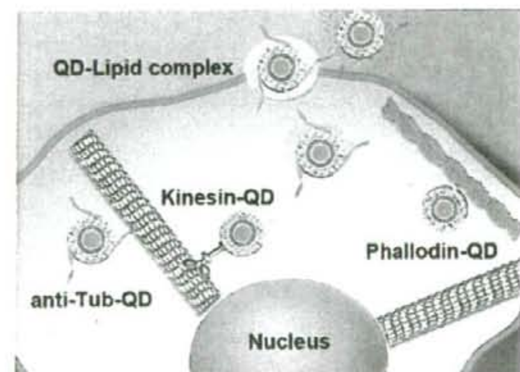

Fig. 1 – A schematic diagram of our intracellular imaging technique. QD–lipid complexes were internalized by the fusion of cellular membrane. Various bioconjugated QDs entered into cytoplasm and the bioactivities were retained in the cells. Phalloidin–QDs and anti-tubulin–antibody–QDs specifically bound to the actin filaments and the microtubules, respectively. Kinesin-QDs moved on the microtubules.

Antibody–QD conjugate

To label microtubules in the living cells, QDs were conjugated to a monoclonal antibody against microtubules. Amino functionalized PEG coated QD 655 (Qdot® nanocrystals, Invitrogen Co.) was linked to anti-bovine α-tubulin mouse monoclonal antibody (isotype IgG1, Molecular Probes). Qdot® Antibody Conjugation Kit (Qdot® nanocrystals, Invitrogen) was used according to manufacturer instructions. The anti-tubulin–QDs were suspended in PBS (pH 7.4) and stored at 4 °C. The final concentration of anti-tubulin–QDs was determined by measuring the absorbance of QDs in the conjugate solution.

Kinesin–QD conjugate

Kinesin-1, 560 amino acids with biotin-tag at C-terminal, from mouse (KIF-5a) was linked to QDs via the streptavidin–biotin reaction. Streptavidin functionalized PEG coated QD 655 (Qdot® nanocrystals, Invitrogen) was conjugated to C-terminal biotinylated kinesin. 5 µl of 1 µM QD solution was diluted by 5 µl of PBS (pH 7.4). Then 30 µl of 1 µM kinesin solution was added to the QD solution and incubated for 20 min at room temperature. The kinesin–QDs were stored at 4 °C.

Internalization of QD-bioconjugates into living cells

Assemblies of QD–lipid complexes were prepared as follows. The bioconjugated QD solution was diluted with 97 µl of serum-free L-15 medium (GIBCO, Invitrogen Co.) to 5 nM, and then 3 µl of lipid reagent (FuGENE® HD, Roche Ltd.) was added directly into the medium containing the diluted QD-bioconjugates. The solution was tapped for mixing, and incubated for 20 min at room temperature. For treatment with the QD–lipid complex, human breast cancer cells, MDA-MB-231 (ATCC Co.), were grown in a glass-bottom dish with L-15 medium containing 10% FBS. The cells were washed with FBS-free L-15 medium, and the culture medium was then exchanged with 1 ml of the FBS-free L-15 medium. The QD–lipid complex was added to the cells (with final concentration of 0.5 nM) and incubated for 3 h. After 3 h of incubation, the cells were washed with PBS buffer to remove the non-binding QD–lipid complex, and then 2 ml of L-15 medium with 10% FBS was added. Observations commenced 2 h after this final addition.

All internalization procedures were performed at 37 °C in an incubator and observed at 35 °C on the microscope except in the QD–kinesin conjugates experiment. In this latter case the QD–kinesin–lipid complex incubation in cells was performed at 27 °C

in FBS-free L-15 medium that contained 1 mM ATP. Observations were performed at 25 °C.

Optical system with confocal microscope

The optical system for two-dimensional observations of fluorescence from QDs consisted primarily of an epi-fluorescent microscopy (IX-71, Olympus) with modifications, a Nipkow disk type confocal unit (CSU 10, Yokogawa), and an electron multiplier type charge-coupled device camera (EM-CCD, Ixon DV887, Andor Technology) [13]. The objective lens (100× UPlanFLN, 1.30 NA, oil, Olympus) was used for phase contrast imaging. QDs were illuminated by a green laser (532 nm wavelength, Crystalaser). The fluorescence from the QDs was filtered (transmission wavelength of the filter was >580 nm; Omega Optics, Austin). Images were taken with the rate of 10 to 30 frames per second.

MSD analysis of single particle movement

To investigate the dynamic behavior of a particle, Mean Square Displacement (MSD) was calculated from x–y coordinates of individual tracking position data [24]. MSD values of individual tracking are defined by the following equation.

$$\mathrm{MSD}(n\Delta t) = \frac{1}{N-n}\sum_{i=1}^{N-n}\left[(x_{i+n}-x_i)^2+(y_{i+n}-y_i)^2\right]$$

where x_i and y_i are positions on frame i, N is the total number of frames. Δt is the time between frames and distance between steps in time t and $n\Delta t$ is the time interval over which the MSD is calculated. Thus MSD is a function of time. To get the information for the diffusion coefficients and the velocities, MSD were fitted by the following equation.

$$\mathrm{MSD}(\Delta t) = 4D\Delta t + V^2(\Delta t)^2 \qquad \lim_{t\to 0}\mathrm{MSD}(\Delta t) = 4D\Delta t$$

where D is diffusion coefficient and V is drift velocity.

When MSD was fitted versus time, the linear plot of MSD produced represents random Brownian movement. When the change in MSD was nonlinear with time, the movement is directed diffusion or confined diffusion. A decreasing slope indicates confined movement. On the other hand, directed diffusion produces an MSD plot with an increasing slope.

Results and discussion

We developed a lipid transfection based delivery method using the transfection reagent, FuGENE® HD. We tested the best condition to introduce QDs without aggregation into cells. The ratio of QD and the FuGENE concentrations is important to deliver many single QDs in cells. Although the higher concentration of FuGENE delivers many QDs into living cells, it is harmful to living cells. Thus the concentration of FuGENE is fixed according to manufacturer instructions, and then various concentrations of QDs were tested to find the best condition for delivery of a lot of single QDs into living cells. The criteria for single QDs without aggregation is that the fluorescence intensity of QD at on-state of blinking [10,13] is within 0.7–1.3 times of single quantum dot intensity measured before mixing with FuGENE. Based on this criteria, we tested three conditions that 97 μl of the 1.5, 5 and 12 nM QD solution mixed with 3 μl of the transfection reagent, and this mixture was diluted 10 times with adding 900 μl of L-15 medium before adding it to the cells (detailed see Materials and Methods). At QD concentration of 12 nM, aggregation of QDs was increased. At QD concentration of 1.5 nM, QD keeps single particle but less number of QDs were internalized. The best condition was obtained at 5 nM QD solution. This was the same to all of types of bioconjugated QDs tested. We have delivered hundreds (100–400) of non-conjugated QDs into a single living cell with the best condition.

The non-conjugated QDs were observed under a Nipkow disk confocal microscope [13]. Hundreds of QDs were delivered into cytoplasm of living cells (Figs. 2A and B) and imaged for 10 min or longer. Their position in living cells was tracked using a previously described single molecule tracking method [13]. Single QDs were moved by random diffusion (Fig. 2B right panel) and they did not aggregate around the nucleus region. The delivered QDs were successfully dispersed as single QDs without forming aggregations in the cytoplasm unlike previous reports [17,18]. This is also in direct contrast to the endocytosis based delivery method of QDs where the QDs formed aggregates in perinucleus region [13,17,25]. These results indicate that the non-conjugated QDs were delivered in cytoplasm without using any coatings such as a vesicle and their movements in the cytoplasm were by diffusion.

To determine if this method could deliver bioconjugated-QDs into cells, we attempted to deliver QDs conjugated with small molecules of phalloidin which specifically bound to the actin filaments. The amino QD655 was specifically cross-linked with amino-phalloidin. Phalloidin–QDs were inserted into the living cells and observed specifically underneath the cell membrane where actin filaments are localized [13] (Fig. 2C upper panel). Tracking of these phalloidin–QDs showed almost no movement even when measurements were taken for 30 s. This is in direct contrast to the random movement of the non-conjugated QDs.

To confirm the specific colocalization of phalloidin–QD conjugates with actin filaments, the cells were treated with cytochalasin D which depolymerizes actin filaments. After 10 min treatment with cytochalasin D, phalloidin–QDs moved randomly with similar movements to non-conjugated QDs (see Supporting information, Fig. S1). We further analyzed quantitatively the dynamics of phalloidin–QDs by cytochalasin D treatment (Fig. S2). Phalloidin–QDs before (79 QDs) and after (93 QDs) cytochalacin D treatment were tracked with video rate of 33 ms and then their average velocities within 10 s were calculated. After 10 min of treatment with Cytochalacin D, the velocities of the half of the QDs were increased. These results indicate that phalloidin–QDs bound to immobile actin filaments become free to move after treatment with cytochalasin D.

A mean square displacement (MSD) analysis was performed to qualitatively measure the overall motion of the QDs including diffusion and directed movement [14,24] as seen in Fig. 3.

The plots of non-conjugated and phalloidin–QDs could be fitted to a linear line representing the diffusion coefficient of random diffusion. The diffusion coefficient for non-conjugated-QDs (n=211 in 4 cells) was 3180 nm^2/s, which is approximately 8 times faster than that of the phalloidin–QDs, 410 nm^2/s. The diffusion coefficients of phalloidin–QD (n=353 in 4 cells) increased when the cell was treated by cytochalacin D. After a 10 min treatment, the diffusion coefficient was 2550 nm^2/s (Fig. S3), which is similar to that of non-conjugated-QDs. This indicates that complexes of

phalloidin–QDs and actin filaments had been released. These results confirm that our intracellular delivery method can indeed be used for specific labeling of living cellular components.

Antibody based imaging is the one of popular methods for specific targeting of various proteins. To test the potential of our intracellular targeting method in wider applications, we attempted to deliver antibody conjugated QDs that bind to targeted cellular components. Microtubules were specifically targeted because they play an important role in a structural support as part of the cytoskeleton and have dynamic behaviors such as polymerization and depolymerization [26]. To label microtubules, QDs were linked to anti α-tubulin antibody (anti-tubulin–QD) which has a specific affinity to a tubulin dimer in the microtubule filaments. Hundreds of the anti-tubulin–QD conjugates delivered to the cell were spread throughout the entire cell cytoplasm (Fig 2D). This is in contrast with phalloidin–QD conjugates which were detected only in the peripheral areas of the cell. Remarkably, the linear traces could be clearly observed when QDs were exposed for 30 s (Figs. 2D and S3). The anti-tubulin–QDs moved directionally with backward and forward movements. The directional movement was supported by MSD plot (n=76 in 3 cells) (Fig. 3). The MSD plot of anti-tubulin–QDs could be fitted to parabolic curves indicating directional movement with an average value of 50.3 nm/s. This is in direct contrast to non-conjugated QDs and phalloidin–QDs. These results also support the directional movement of

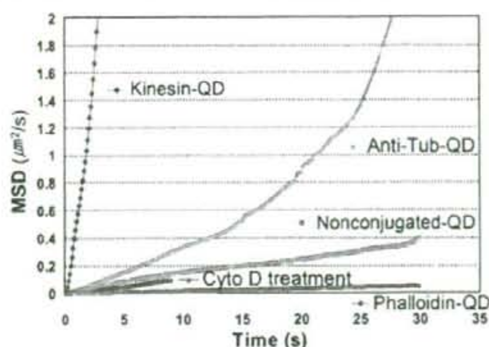

Fig. 3 – MSD plots of various bioconjugated QDs. While non-conjugated-QDs show the linear plot indicative of a random diffusion with D=3180 nm^2/s (linear fitting with R^2=0.968), phalloidin–QDs indicate the slow movement of actin filaments (D=410 nm^2/s, R^2=0.994). In the 10 min treatment of cytochalasin D, the diffusion coefficient of phalloidin–QDs became to the random diffusion, D=2550 nm^2/s (R^2=0.9677, observation in 33 ms, video rate). The MSD plots of kinesin–QDs and anti-tubulin–QDs exhibit the directional movement in their dynamic behaviors by increasing their slopes. The average velocities calculated from the curve were 457 nm/s for kinesin (R^2=0.962), and 50.3 nm/s for microtubules (R^2=0.972).

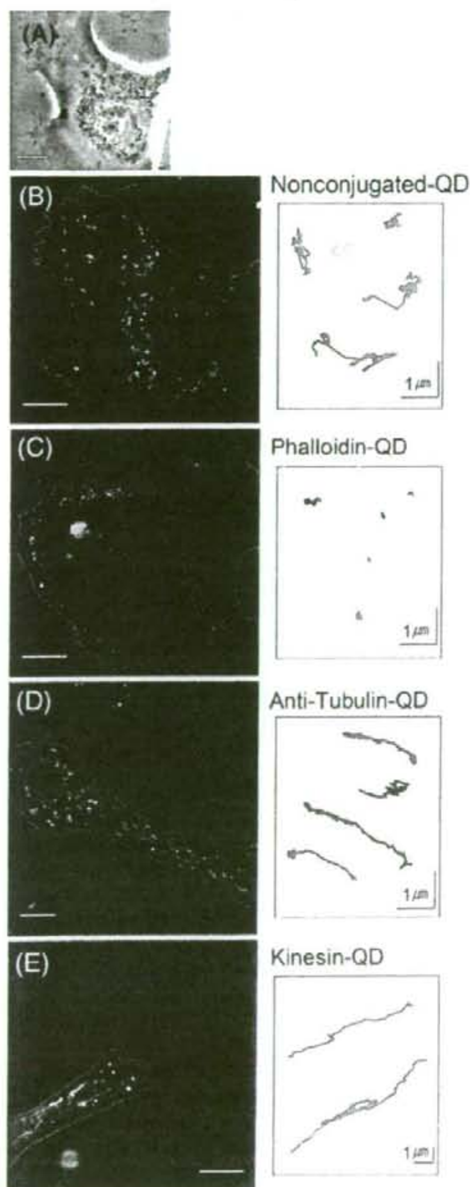

Fig. 2 – Intracellular delivery of the various types of bioconjugated QDs in living cells. (B)–(E) Left panels are the fluorescence images of QDs with a 0.1 s exposure time. Blue line is the trajectory of each QD for 30 s and the orange dotted line represents the cell membrane and nucleus. Right panels are the magnified views of each trajectory. (A) Phase contrast image of the living cell of (B) as a fluorescence image. (B) Fluorescence image of non-conjugated-QDs. The trajectories in the right panel had a random shape. (C) Trajectories of phalloidin–QDs. They showed the specific binding to actin filaments. (D) Trajectories of anti-tubulin-QDs. The trajectories displayed the dynamics of microtubules. (E) Fluorescence image of kinesin-QDs. The linear trajectories were indicative of directed motions of kinesin motors. White scale bars, 10 μm.

microtubules. The directional movement possibly derives from the dynamics of microtubules [26].

If QDs are delivered not by the intracellular delivery but by endocytosis, they still exhibit directional movement towards the nucleus region by vesicle transport on the microtubules [13,27]. Thus it is critical to determine whether the QDs were binding to microtubules or being transported in vesicles. To confirm the QDs were specifically targeting microtubules, cells were incubated with anti-tubulin–QD conjugates for 30 h. This provided sufficient time for endocytosed QDs to aggregate in the perinucleus region by motor protein transport [13]. However, after this long incubation time, the QDs did not form aggregates around the nucleus. Instead, they remained dispersed throughout the cell cytoplasm specifically binding to the microtubules (Fig. S4). This result indicates that the antibody–QD conjugates had been delivered into the cytoplasm without any coating and they retained their ability to bind to specific target proteins in the living cells.

In order to demonstrate how powerful our intracellular delivery method is, we delivered purified motor protein-conjugated QDs into the cytoplasm and traced the movement of QDs to investigate behavior of a purified protein in living cells. Avidin–QDs were conjugated to a biotinylated recombinant motor protein, kinesin-1, using an avidin–biotin coupled reaction. Kinesin walks along a microtubule from its minus to plus end in a living cell [3]. Kinesin–QD conjugates were incubated with the lipid reagent and added to the cultured cells. Similar to the other conjugates, kinesin–QD conjugates did not form large aggregations, instead they were spread evenly throughout the cytoplasm. Fig. 2E shows the results for single particle tracking of kinesin–QDs. The majority of the QDs were moving in these images. As expected, kinesin–QDs moved both linearly and directionally. Detail analysis, however, revealed QDs exhibited stop and back movements along the same track (Fig. 2E). Using the *in vitro* motility assays on a cover slip [3,28,29], purified kinesin moved smoothly and continuously along microtubules in contrast to irregular movement of kinesin in cell as discussed later. This suggests that there must be unknown factors that regulate the intracellular movement of kinesin in living cells.

The movements of kinesin–QD were analyzed using a MSD method (Fig. 3). The plots ($n=20$ in 5 cells) were well fitted to parabolic curves, indicating directional movement towards the cell membrane driven by kinesin. The average velocity of kinesin that

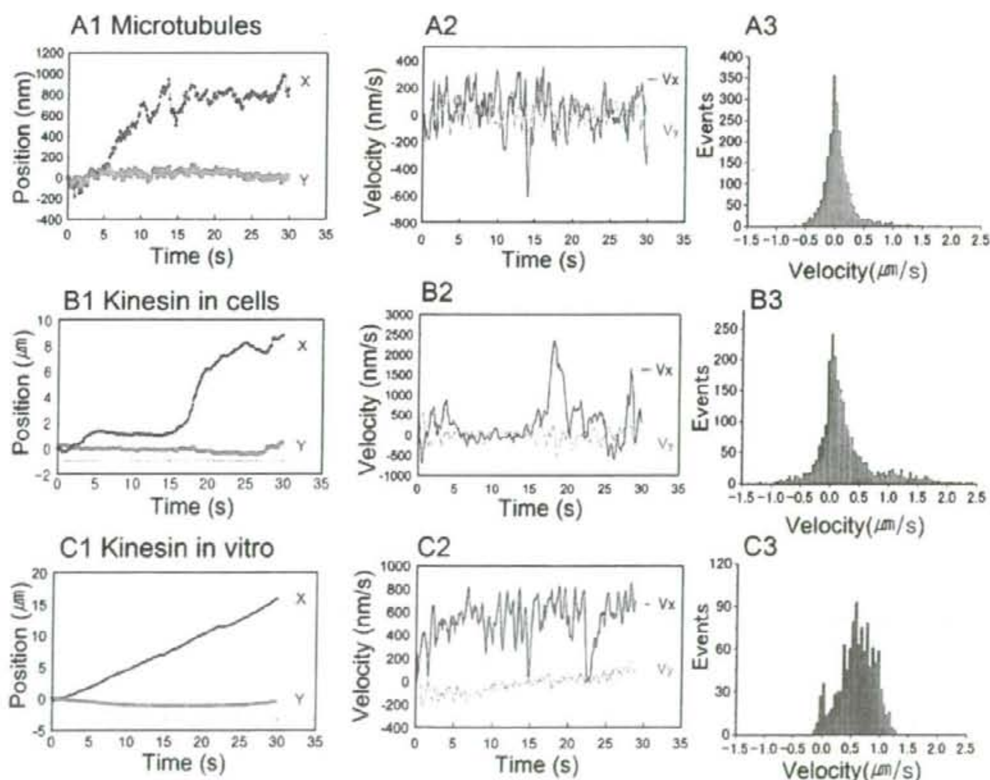

Fig. 4 – Trajectory analysis of the dynamics of (A) microtubules, (B) kinesin in cells and (C) kinesin *in vitro*. First column is the x, y position plots versus time. It exhibits the directionality in the X axis (transverse direction of microtubule filament). Second column is the plot of the velocity in the X (V_x) and Y axes (V_y). The third column is the X axis velocity (V_x) distributions of (A) microtubules, (B) kinesin in cells and (C) kinesin *in vitro*. Distributions were generated by 12 QDs tracking of microtubules targeting ($n=2304$ events), 11 QDs tracking of kinesin in cells ($n=2328$) and ten QDs tracking of kinesin *in vitro* ($n=1130$).